Imaging Near Metal with a MAVRIC-SEMAC Hybrid

K. M. Koch,[1]* A. C. Brau,[2] W. Chen,[2] G. E. Gold,[3] B. A. Hargreaves,[3] M. Koff,[4] G. C. McKinnon,[1] H. G. Potter,[4] K. F. King[1]

The recently developed multi-acquisition with variable resonance image combination (MAVRIC) and slice-encoding metal artifact correction (SEMAC) techniques can significantly reduce image artifacts commonly encountered near embedded metal hardware. These artifact reductions are enabled by applying alternative spectral and spatial-encoding schemes to conventional spin-echo imaging techniques. Here, the MAVRIC and SEMAC concepts are connected and discussed. The development of a hybrid technique that utilizes strengths of both methods is then introduced. The presented technique is shown capable of producing minimal artifact, high-resolution images near total joint replacements in a clinical setting. Magn Reson Med 65:71–82, 2011. © 2010 Wiley-Liss, Inc.

Key words: MRI of arthroplasty; metal implants; image artifacts, 3D imaging

INTRODUCTION

The soft-tissue contrast attainable with magnetic resonance (MR) imaging techniques is advantageous in diagnosing complications from arthroplasty procedures (1–3). Unfortunately, conventional MR images are significantly compromised by implant-induced susceptibility artifacts. Metal-induced B_0 perturbations are orders of magnitude larger than those induced by anatomic susceptibility boundaries. These increased perturbations dramatically disrupt the spatial-encoding mechanisms applied in conventional MR imaging.

A number of hardware and software solutions have been proposed to mitigate MR image distortions near metal implants. Such approaches include single-point imaging (4), prepolarized MRI (5), view-angle tilting (VAT) (6,7), and dual-reversed-gradient acquisitions (8). Existing challenges and limitations have prevented widespread adoption of these techniques in the clinical arena.

The recently described multi-acquisition with variable resonance image combination (MAVRIC) and slice-encoding metal artifact correction (SEMAC) methods have been shown to significantly reduce susceptibility artifacts near metal implants (9,10). By relying on conventional imaging techniques that can be applied on standard clinical MR hardware, the MAVRIC and SEMAC methods offer a pathway to low-artifact clinical MR imaging near a wide variety of metal implants. Measurements of artifact reduction near a total knee replacement at 1.5 T have found that MAVRIC and SEMAC both reduce image distortions by roughly a factor of 10 when compared with 2D-FSE images (11). Both techniques have also been demonstrated to be capable of revealing pathology not accessible via standard MR imaging methods (12,13).

Although MAVRIC and SEMAC approach the susceptibility artifact problem from different perspectives (SEMAC from a 2D slice-selective approach and MAVRIC from a 3D approach), they mitigate susceptibility artifacts using similar physical principles. Here, we describe the connection between the two methods and elaborate on the nuanced differences between them. After highlighting the theoretical principles behind the MAVRIC and SEMAC techniques, the spectral properties by the two methods are analyzed in detail. A hybrid sequence possessing advantageous elements of both techniques is then presented. Finally, this hybrid method is demonstrated on arthroplasty patients in a clinical setting and is compared with existing standard-of-care clinical images.

THEORY

Susceptibility Artifacts: Spectral and RF Considerations

In the presence of an off-resonance frequency distribution $\Delta\nu_0(x,y,z)$, the frequency-encoded dimension (x) in a conventional spin-warp image is distorted according to

$$\rho(x,y,z) \xrightarrow{\Delta\nu_0(x,y,z)} \rho\left(x - \frac{2\pi\Delta\nu_0(x,y,z)}{\gamma G_x}, y, z\right), \quad [1]$$

where G_x is the amplitude of the applied frequency-encoding gradient. Stepped phase-encoding dimensions in a spin-warp image are not susceptible to distortions from off-resonance effects. For notational simplicity, logical (x,y,z) coordinates will be used throughout this work to represent the (read, phase, slice/phase)-encoded directions.

Frequency-encoding gradient amplitudes are not only constrained by hardware limitations but are also determined by the desired readout field of view (FOV_x) and the chosen reception bandwidth (BW_r, given in Hz),

$$G_x = 2\pi\frac{\mathrm{BW}_\mathrm{r}}{\gamma\mathrm{FOV}_x}. \quad [2]$$

For a readout of 256 samples collected at a relatively high sampling (readout) bandwidth of $\mathrm{BW}_\mathrm{r} = \pm 125$ kHz (1 kHz/pixel), each 1 kHz of $\Delta\nu_0$ offset corresponds to roughly 1 pixel of spatial displacement. It is not uncommon to encounter off-resonance values of 10–15 kHz near

[1]Applied Science Laboratory, GE Healthcare, Waukesha, Wisconsin, USA
[2]Applied Science Laboratory, GE Healthcare, Menlo Park, California, USA
[3]Department of Radiology, Stanford University, Palo Alto, California, USA
[4]Department of Radiology, Hospital for Special Surgery, New York, New York, USA

*Correspondence to: Kevin M. Koch, Ph.D., GE Healthcare, Applied Science Laboratory, 3200 N. Grandview Blvd, W875 Waukesha, WI 53188; E-mail: kevin.koch@ge.com

Received 31 March 2010; revised 31 March 2010; accepted 1 May 2010.
DOI 10.1002/mrm.22523
Published online 27 October 2010 in Wiley Online Library (wileyonlinelibrary.com).

implanted metal hardware, which thus correlates to distortions at the 10–15 pixel level in high readout bandwidth acquisitions.

The spectral bandwidth ($\delta\nu_{RF}$) of applied RF pulses determines the maximum off-resonance frequency encountered in a spatial-encoding process. It is common to use Carr-Purcell-Meiboom-Gill (CPMG) spin-echo-based imaging sequences near metal implants. In this work, the term Fast-Spin-Echo (FSE) will be used to refer to this class of imaging sequence. Such sequences allow for rapid acquisition of T_2^*-refocused signal, which is of particular importance in the presence of strong $\Delta\nu_0$ gradients. The bandwidths of refocusing RF pulses used in such sequences are limited by peak amplitude of (excitation) radio frequency field and energy absorption considerations. Typically, maximum applied bandwidths are in the 2-kHz range. Thus, the maximum effective off-resonance value for a spin encountered in the experiment is only $\approx \pm 1$ kHz; the other spins are simply not excited.

From a frequency-encoding perspective, slice-selection processes widen effective spectral windows and thus introduce additional encoding distortions. Consider a spin that is $\Delta\nu_0 = 10$ kHz off-resonance. Without slice selection, this spin would be outside of the RF bandwidth used in a CPMG imaging process. However, if a slice-selection gradient, G_z, is applied to excite slices of thickness $\delta z = 2\pi\delta\nu_{RF}/(\gamma G_z)$, this spin could be brought back into the RF bandwidth for a slice that is centered a distance of $\Delta z = \delta z \cdot 10\,\text{kHz}/\delta\nu_{RF}$ away from its true z-position. As the slice-selective gradient is turned off during signal acquisition, the spin is (a) misregistered to the wrong slice in the z-dimension and (b) frequency-encoded to an incorrect position given by Eq. 1. If $\delta\nu_{RF} = 2$ kHz RF pulses were used, the slice-selection process enables this spin to be distorted in the frequency-encoded dimension 10 times farther than any spin could be distorted in the absence of slice selection.

VAT is a process that was introduced to eliminate this effect (14). The basic principle of VAT is to apply the slice-selection gradient that was used during RF application again during the acquisition window. Such an approach allows for 2D slice-selective imaging while removing the aforementioned amplification of frequency-encoded distortions. The tradeoffs to VAT are (1) a slight shear of the slice in the logical x–z plane by the view-angle $\theta_{VAT} = \text{atan}\left(\frac{G_z}{G_x}\right)$ and (2) the introduction of an acquisition window filter

$$F(t) = \text{sinc}(\gamma G_z t \delta z/2), \quad [3]$$

which can blur acquisitions with long readout windows (14).

As a stand-alone method, the VAT technique is of limited value near most metal implants because of its vulnerability to slice-selective distortions. As discussed in detail by Lu et al. (10), the $\Delta\nu_0(x,y,z)$ distributions induced by metal implants can significantly alter intended slice planes from their intended geometry. Briefly, a spin will be misregistered in the slice-selective dimension by one slice-width for every $\delta\nu_{RF}$ kHz for which it is offset from the resonance frequency. For example, when using 2-kHz RF pulses, a spin at 10 kHz will be misregistered in the slice dimension by five slice widths. For a slice-selective image, Eq. 1 can be modified to account for these additional distortions:

$$\rho(x,y,z) \xrightarrow{\Delta\nu_0(x,y,z)} \rho\left(x - \frac{2\pi\Delta\nu_0(x,y,z)}{\gamma G_x}, y, z - \delta z\frac{\Delta\nu_0(x,y,z)}{\delta\nu_{RF}}\right), \quad [4]$$

Although postprocessing correction of slice-selective distortions has been proposed by Pauly et al. (15) and Skare et al. (8), such corrective measures are limited in scope. In particular, any postprocessing shifting of pixels in regions with strong $\left|\frac{\partial\Delta\nu_0(x,y,z)}{\partial z}\right|$ trends will be of limited accuracy.

The most robust manner of mitigating slice-selective distortions is to instead phase encode the z-dimension. However, such an approach is not without its own problems. The spectral coverage of a conventional z-phase-encoded approach is given by $\delta\nu_{RF}$, whereas that of a slice-selective experiment is $N\delta\nu_{RF}$, where N is the number of slices. Although many of the spins in the slice-selective imaging volume are misregistered in both the frequency-encoded and slice-selective dimension, they are at least included in the image. A single z-phase-encoded image will have a large signal void where spins outside of the limited RF bandwidth are resonating, whereas the slice-selective image will not have these signal voids at the expense of a severely distorted image.

MAVRIC and SEMAC

The MAVRIC method is based on 3D-FSE imaging techniques. As previously discussed, conventional 3D-FSE images have limited spatial coverage near metal implants because of off-resonance spins being excluded from the imaging process. Therefore, MAVRIC acquires multiple 3D-FSE images at incremented offsets of transmission and reception frequencies. Similar to a 2D multislice acquisition, multiple spectrally unique echo trains can be interleaved within each repetition time of a MAVRIC acquisition. MAVRIC spectral images, or "bins," are independently reconstructed to produce volumetric images (9). Around commonly encountered metal implants, spectral bins spanning of ± 12 kHz are sufficient to capture the available MR signal. Any remaining signal beyond this spectral band would not be imaged by the MAVRIC acquisition. As MAVRIC does not apply any selection gradients, the technique does not restrict signal in the z-dimension—which conventional 3D-FSE acquisitions accomplish via slab-selection techniques. Thus, to prevent through-plane aliasing, MAVRIC requires the use of surface coils to restrict active signal in the z-dimension.

The imaged volume in a given MAVRIC spectral bin is determined by the $\Delta\nu_0$ distribution induced by the metal device. Instead of the Cartesian slabs excited in a slice-selective experiment, MAVRIC spectral images are 3D isocontours of the implant-induced ν_0 distribution. Each of these volumetric images is free of slice distortions and possesses minimal frequency encoded distortions (dictated by the applied RF bandwidth). The independent spectral bin images are combined via quadrature summation to form a composite image.

SEMAC begins with a slice-selective VAT image, but adds phase encoding along the z-dimension to spatially resolve distorted slice planes (10). Thus, a given slice volume is excited M times to resolve M z-encoded positions within the excited volume. Frequency-encoded distortions are limited in SEMAC images because of the use of VAT. SEMAC does not z-phase encode the entire imaged volume, but instead encodes a smaller subvolume centered on excited slice volumes. This minimizes the number of z-encodes needed to adequately register slice distortions. The number of encodes needed per slice volume depends on anticipated off-resonance contributions. SEMAC typically uses 16 encodes with 2-kHz RF pulses, which can register off-resonance contributions of up to ±16 kHz. Spectral contributions resonating beyond this band will be aliased (misregistered) in the z-dimension of a SEMAC acquisition.

The readout filter introduced by the VAT process (Eq. 3) is mitigated in SEMAC through the use of a high readout bandwidth (±125 kHz). For the slice-selection processes used in SEMAC ($\gamma G_z \delta z/2\pi = \delta\nu_{RF} = 2$ kHz), readout windows of 1–1.5 ms (256–384 samples) do not result in significant blurring of resulting images.

Although a complex summation process was introduced in Ref. 10, high-resolution SEMAC images require quadrature summation to preserve SNR. Under this reconstruction formalism, 3D-resolved images for each excited slice volume acquired using the SEMAC technique are independently reconstructed and then registered with one another in the z-dimension before undergoing quadrature combination.

Despite their differing approaches, the underlying connection between the MAVRIC and SEMAC techniques is straightforward. Both techniques excite multiple spectral bands separated by incremented offsets. Both techniques frequency encode one dimension and phase encode the other two dimensions of each excited volume. By using the same z-selection gradient amplitude during both excitation and readout (MAVRIC uses no selection gradients, whereas SEMAC uses VAT), both techniques limit frequency-encoded off-resonance contributions to those contained within the RF bandwidth (7). Given these similarities, if identical z-encodings and spectral properties were used in both techniques, SEMAC could simply be considered MAVRIC with the added application of a static "Z-shim".

MAVRIC and SEMAC acquisitions can both be accelerated using autocalibrated parallel imaging methods such as Autocalibrated Reconstruction of Cartesian data (ARC) (16,17), which has been demonstrated compatible with imaging near metal implants (18,19). Both techniques can also be accelerated using partial-Fourier techniques in the k_y-encoded dimension. Partial-Fourier techniques are applicable near metal implants when using spin-echo-based imaging methods because of the refocused signal acquired at each k_y position. Elliptical sampling of the $k_y - k_z$ phase-encoded plane (i.e., corner cutting) can also be used to reduce image acquisitions by 25% (20).

Artifacts and Spectral Properties

Both MAVRIC and SEMAC combat susceptibility artifacts near metal implants by breaking large spectral dispersions into smaller spectral bins that can be frequency encoded with reduced spatial distortions. There are two regimes of encoding errors in such spectrally segmented strategies. The first regime is composed of bulk shifts of spins on a very small length scale (typically on the sub or single pixel level). In an individually reconstructed SEMAC or MAVRIC spectral bin image, such shifts are nearly invisible to the naked eye.

The second regime of encoding errors is encountered when the implant-induced $\Delta\nu_0$ distribution has rapid spatial variation in the frequency-encoded dimension. These artifacts become prominent when the magnitude of the induced gradient approaches or surpasses that of the applied frequency-encoding gradient. A further degree of complication is introduced when the nonuniform response of spins to off-resonance radiation (i.e., the spectral magnitude profile) is taken into account.

Consider a single frequency-encoded line (x) of an individual spectral bin, b. Beginning with the distortion model presented in Eq. 1, we include the effect of spectral bin offsets:

$$\Delta\nu_b(x) = \Delta\nu_0(x) - \nu_0^b, \qquad [5]$$

where ν_0^b is the spectral offset of the given bin. We also introduce the spectral profile function $F(\nu)$. Using these parameters, the intensity of the bth spectral bin image can be expressed as follows:

$$I(x,b) = \rho\left(x - \frac{2\pi\Delta\nu_b(x)}{\gamma G_x}\right) \cdot F[\Delta\nu_b(x)]. \qquad [6]$$

The differing effects of $\Delta\nu_0$ gradients on reconstructed images can be isolated by taking a spatial derivative of Eq. 6:

$$\frac{\partial I(x,b)}{\partial x} = \frac{\partial\rho(x')}{\partial x'} \cdot \left(1 - 2\pi\frac{\partial\Delta\nu_b(x)/\partial x}{\gamma G_x}\right) \cdot F[\Delta\nu_b(x)] + \rho(x') \cdot \frac{\partial\Delta\nu_b(x)}{\partial x}\left.\frac{\partial F}{\partial\nu}\right|_{\nu=\Delta\nu_b(x)}, \qquad [7]$$

where $x' = x - \frac{2\pi\Delta\nu_b(x)}{\gamma G_x}$.

In the absence of $\Delta\nu_0$ perturbations, the right-hand side of Eq. 7 reduces to $\partial\rho/\partial x$, which is the result expected from inherent image contrast. However, when $\Delta\nu_0$ perturbations are taken into account, additional spatial intensity variations are introduced in the image. The first term in Eq. 7 accounts for intensity disruptions resulting from local perturbation gradients that are large when compared with the applied frequency-encoding gradient, G_x. These artifacts fall into the previously discussed "second regime" of encoding errors occurring when the condition

$$\gamma|G_x| \gg 2\pi\left|\frac{\partial\Delta\nu_0}{\partial x}\right| \qquad [8]$$

is violated. The image signal in such regions represents either (a) integration of the effective spin density across regions where $\gamma G_x \approx -2\pi\frac{\partial\Delta\nu_0}{\partial x}$ or (b) a reduction in signal due to the effective encoded voxel approaching zero size. These two cases represent the local negation and exacerbation of the frequency-encoding gradient, respectively, when it is superimposed with the implant-induced frequency distribution.

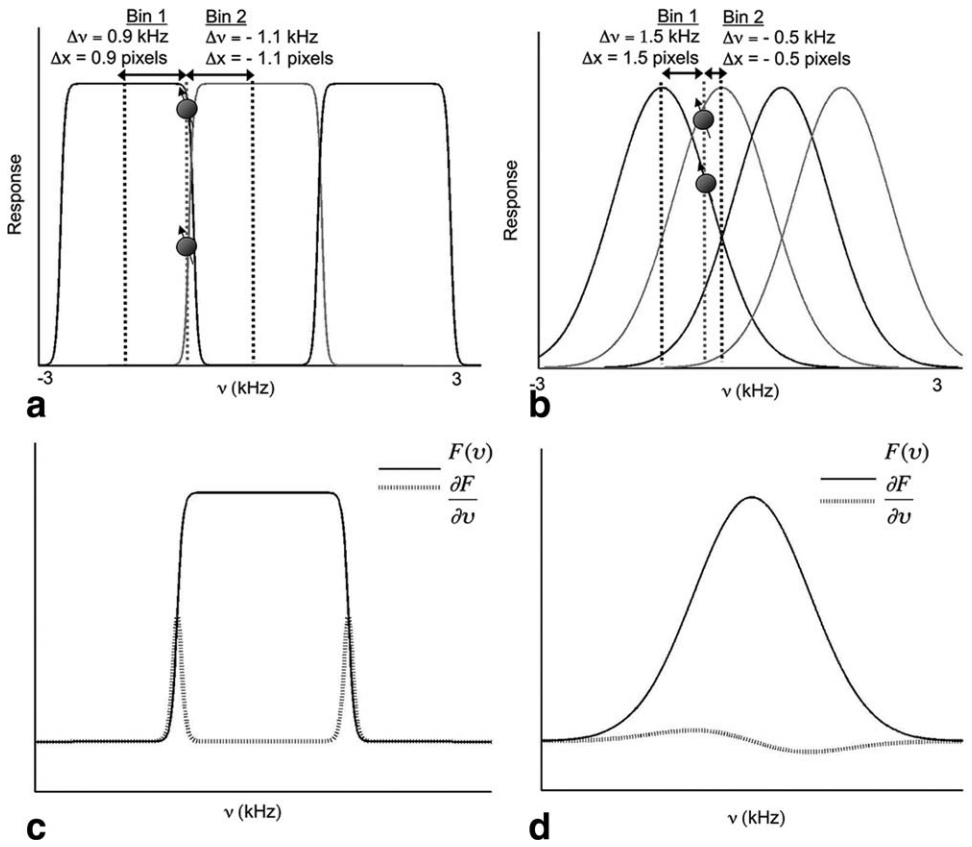

FIG. 1. Choices of spectral arrangement strategies: (**a**) closely aligned box-car spectral profiles and (**b**) overlapping Gaussian spectral profiles. The effect of spectral profile choice on the second term of Eq. [7]: (**c**) box-car profile and (**d**) Gaussian profile.

The second term in Eq. 7 convolves local perturbation gradients and nonuniform spectral responses. The contribution of the spectral derivative $\frac{\partial F}{\partial \upsilon}$ acknowledges that spins being pushed through an inhomogeneous spectral response will result in additional spatial intensity artifacts. The scaling of this term by the local perturbation gradient demonstrates that this effect also depends on the rate of field variation.

A challenge with both the MAVRIC and SEMAC methods is how to smoothly combine separately encoded spectral bins, each of which inevitably contains the spatial intensity artifacts represented by Eq. 7, to form a composite image spanning the entire spectral dispersion.

Broadly speaking, there are two spectral strategies from which to choose. Figure 1a, b presents these two strategies. In (a), highly selective box-car spectral responses are closely aligned with one another. A quadrature sum of the responses will produce a largely uniform response over the entire spectral dispersion spanned by the bins. The arrangement presented in (b) uses smoothly varying and strongly overlapping responses (gaussian responses are used in this work) that, when properly spaced relative to one another, can also provide a relatively uniform response after quadrature summation. For identical imaging parameters (repetition time, echo time, flip-angle, etc.), this strategy produces composite images that have higher SNR than images constructed with the strategy in (a) because of an averaging effect of the strongly overlapping spectral profiles.

Either strategy presented in Fig. 1 will have intensity artifacts resulting from the first term in Eq. 7. Removing such effects is beyond the scope of the work presented here. However, an iterative reconstruction technique relying on the smooth spectral overlap strategy (b) has been demonstrated in concept and shown to dramatically reduce the intensity artifacts caused by rapid field variations (21).

The dependence of the second term on $\partial F/\partial \nu$ results in a stronger artifact contribution from the tightly arranged spectral strategy presented in Fig. 1a. This is because the edges of such spectral profiles have more rapid $\partial F/\partial \nu$ variations, which is demonstrated in Fig. 1c. As illustrated in (d), the smoother Gaussian responses have a significantly lower rate of spectral variation and therefore show a reduced contribution from this effect.

Spins resonating in overlapping spectral regions will be imaged multiple times. As demonstrated in Fig. 1a, b, these spins will be distorted in opposite directions for adjacent bins. This effect can exacerbate the high-frequency intensity artifacts characterized by Eq. 7. In addition, while the smooth overlap strategy shown in Fig. 1b, d possesses fewer rapidly changing intensity artifacts, it does suffer significant composite image blurring from this opposing-displacement effect. The encoding distortions generating this blur were earlier classified as "first-regime" distortions. Although such shifts cannot be perceived in individual bins, the blur they generate in composite spectrally summed images is easily identifiable. This blurring effect

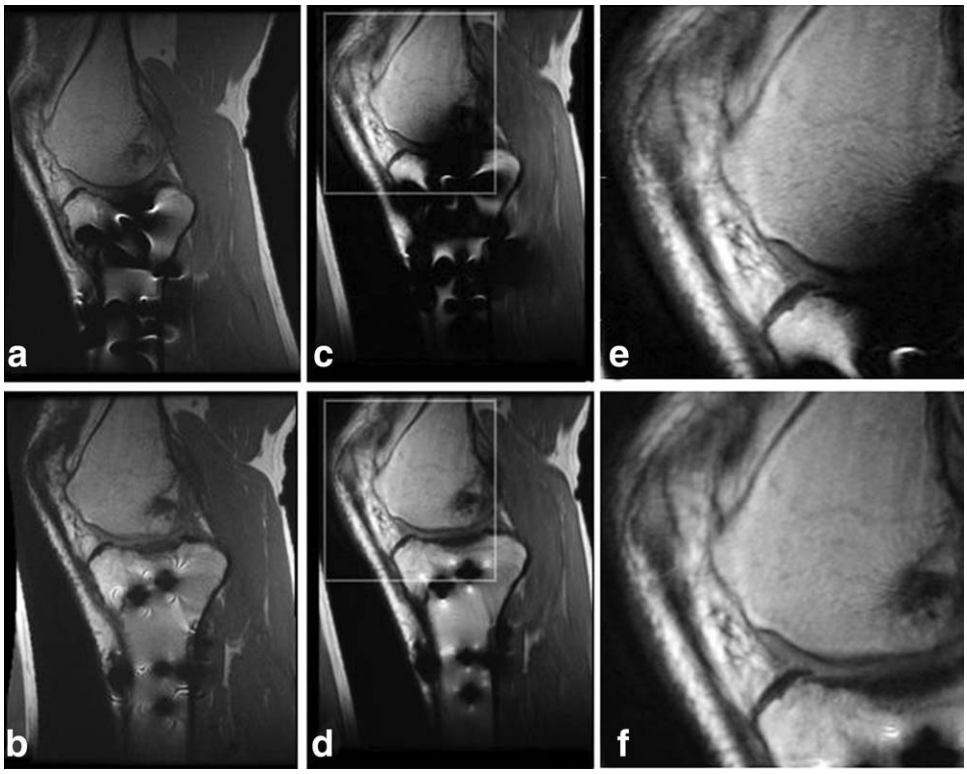

FIG. 2. (**a**) 2D-FSE, (**b**) SEMAC, (**c**) 3D-FSE, (**d**) MAVRIC, (**e**) indicated zoomed region in (**c**), (**f**) indicated zoomed region in (**d**).

is global (i.e., not localized to the implant) and can significantly impact the effective composite resolution of high-resolution acquisitions.

The spectral strategies presented in Fig. 1 are theoretical constructions using ideal spectral profiles. In reality, MAVRIC applies a strategy resembling that presented in Fig. 1b using a Kaiser-Bessel filter in the Shinnar-Le Roux pulse-design algorithm (22) to approximately generate a Gaussian spectral response. SEMAC uses an approach approximating that presented in Fig. 1a. However, it is difficult in practice to generate high bandwidth spin-echo refocusing pulses with the narrow and well-behaved transition band presented in Fig. 1a. Therefore, in practice, SEMAC spectral profiles will have more overlap and a smoother $\frac{\partial F}{\partial v}$ profile than the analyzed idealized box-car strategy.

Figure 2 demonstrates the varying practical consequences of the spectral strategies used by MAVRIC and SEMAC. Images were acquired at 1.5 T using an eight-channel transmit-receive knee coil on a knee fitted with multiple stainless steel screws. Imaging parameters for the displayed images are presented in Table 1. Figure 2a presents a high readout bandwidth ($BW_r = \pm 125$ kHz) 2D-FSE image displaying significant distortions near the stainless steel screws. The SEMAC image displayed in Fig. 2b clearly resolves most of the readout and slice-selective distortions identified in (a). A 3D-FSE image (collected as the on-resonance spectral bin in a MAVRIC acquisition) is presented in (c). The signal loss suffered near metal implants using a conventional 3D imaging strategy is plainly evident. The MAVRIC image presented in (d) is able to recover this missing signal with minimal artifact introduction.

Notice that the 3D-FSE image in Fig. 2c does have some intensity artifacts (particularly on the dipolar magic angles of the signal dropout regions). These are intensity variations caused by the first term in Eq. 7, which do carry through into the composite MAVRIC image in (d). Such artifacts are to be expected in both the MAVRIC and SEMAC images. However, comparison of Fig. 2b, d shows stronger intensity lines in the SEMAC images, which result from the added bin combination artifacts stemming from the second term in Eq. 7. Although MAVRIC images do not suffer as prominently from these second-term artifacts, they do show a global blurring effect that is demonstrated in (e) and (f). Close inspection of the indicated zoomed images from the on-resonance 3D-FSE (e) and MAVRIC (f) acquisitions shows that the MAVRIC image has a broader point spread.

When compared with the conventional images in (a) and (c), both MAVRIC and SEMAC are clearly able to dramatically reduce susceptibility artifacts. The residual intensity artifacts seen in MAVRIC and SEMAC images primarily result from spins being slightly misencoded in the frequency-encoded dimension. Although the magnitude of these distortions are typically on the single-pixel or sub-pixel level, the above analysis shows that they can have a noticeable effect on composite image quality.

Removal of Blurring from Bin Overlap

In this work, the overlapping spectral bin strategy of the MAVRIC technique is used. A method to mitigate the resulting image blur using spectral information inherent to such acquisitions is now presented.

Table 1
Scan Parameters

Case	Method	Plane	FOV (x, y) (cm)	(N_x, N_y)	δz (mm)	N_z	N_A	TE (ms)	TR (s)	ETL	T_{ACQ} min:s
1	2D-FSE	Sag	(20,15)	(320,192)	3	36	2	6.4	3.0	8	5:24
	SEMAC	Sag	(20,15)	(320,192)	3	32	1	9.3	2.5	8	8:58
	MAVRIC	Sagl	(20,15)	(320,192)	3	38	1	7.2	2.5	20	10:31
2	2D-FSE	Cor	(27,19)	(320,204)	3	40	2	41.0	2.5	24	4:31
	MAVRIC	Cor	(27,19)	(320,204)	3	40	1	40.8	2.5	24	6:58
	VS-3D-MSI	Cor	(27,19)	(320,204)	3	40	1	40.8	2.5	24	6:58
3	2D-FSE	Cor	(25,12.5)	(320,160)	3	44	2	38.2	3.0	24	2:49
	MAVRIC	Cor	(25,12.5)	(320,160)	3	44	1	40.0	3.0	24	6:52
	VS-3D-MSI	Cor	(25,12.5)	(320,160)	3	44	1	40.0	3.0	24	6:52
4	MAVRIC	Cor	(22,22)	(256,192)	4.2	32	1	41.3	4.0	24	10:21
5	2D-FSE	Cor	(22,22)	(512,352)	4.0	24	5	26	4.2	22	5:42
	VS-3D-MSI	Cor	(22,22)	(320,256)	4.2	28	1	43.0	4.0	24	11:57
6	2D-FSE	Obl Sag	(20,20)	(512,320)	2	20	4	14.2	4.9	20	5:19
	VS-3D-MSI	Obl Sag	(20,20)	(512,256)	3.2	28	1	39.5	4.8	24	11:58

(N_x, N_y, N_z) represents the acquisition grid, N_A is the number of averages, δz is the slice width or z-encode resolution, and T_{ACQ} is the total acquisition time. Implant cases: (1) knee screws (Figs. 2 and 3); (2) THA phantom (Fig. 4); (3) ankle screws (Fig. 5); (4) clinical THA A (Fig. 6); (5) clinical THA B (Fig. 6); (6) clinical TSA (Fig. 7).

The overlapping Gaussian spectral windows $G_b(\nu)$ used in MAVRIC are constructed such that

$$\sum_{b=1}^{B} G_b(\nu) \approx 1 \quad \forall \nu, \qquad [9]$$

which produces a relatively uniform spectral response across the imaged spectral dispersion.

This property of the MAVRIC acquisition allows field map estimations through a simple weighted average of the magnitude images, $I_b(x, y, z)$. First, the spectral bin image magnitudes are normalized at each pixel location,

$$\sum_{b=1}^{N_b} I_b(x, y, z) = 1 \quad \forall x, y, z. \qquad [10]$$

Using these normalized image intensities, a weighted average field map solution can be estimated as follows:

$$\Delta\nu_0(x, y, z) = \sum_{b=1}^{N_b} I_b(x, y, z) \cdot \nu_0^b. \qquad [11]$$

Field maps are estimated using this procedure with much greater precision than the separation between the spectral bins (typically 1 kHz). This additional spectral information is extracted from the known homogeneous spectral response of the composite MAVRIC image. Thus, the motivation for using the overlapping Gaussian profiles (a smooth composite image construction) is precisely the reason that such field maps can be constructed with sufficient precision.

Using these field maps, subimages can be spatially corrected relative to one another in the frequency-encoded dimension. Each pixel in each subimage experiences a net frequency offset, $\Delta\nu_b(x, y, z)$, previously represented in one dimension by Eq. 5, but reproduced here to include all spatial dimensions:

$$\Delta\nu_b(x, y, z) = \Delta\nu_0(x, y, z) - \nu_0^b. \qquad [12]$$

A given subimage $I_b(x, y, z)$ can then be repaired according to

$$I_b(x, y, z) \longrightarrow I_b\left(x - \frac{\Delta\nu_b(x, y, z)}{\mathrm{BW_r}}, y, z\right). \qquad [13]$$

Relative to the severe $\Delta\nu_0$ distributions found near metal hardware, the majority of pixels in an image experience relatively homogeneous distribution. Therefore, much of the shifting needed to remove the blurring effect is large-scale bulk shifting of one image relative to another. The images presented here use nearest-neighbor pixel interpolation when applying this bin-specific correction procedure. More sophisticated interpolation schemes could be applied to gain incremental improvements in performance.

After correcting each subimage using Eq. 13, quadrature summation can be used to produce an image with a significant reduction in spectral overlap–induced blurring.

Hybrid Approach

The spectral overlap strategy used by MAVRIC provides a smooth bin combination procedure and much needed SNR when considering the undersampling schemes needed to accelerate MAVRIC and SEMAC. With the application of the previously described deblurring correction, MAVRIC's spectral strategy can produce high SNR, high-resolution images near metal implants with minimal residual artifacts. However, MAVRIC is challenged in cases where coil sensitivities cannot provide adequate volume selectivity. Particularly in hip and shoulder arthroplasty cases, MAVRIC's lack of slice (or slab) selectivity has resulted in significant aliasing in the z-encoded dimension. Such aliasing can easily compromise the diagnostic quality of MAVRIC images, despite their high SNR and low residual artifacts. Therefore, a more advantageous method would have the z-selectivity of SEMAC and the spectral properties of MAVRIC. A procedure is now described to construct such a hybrid acquisition sequence.

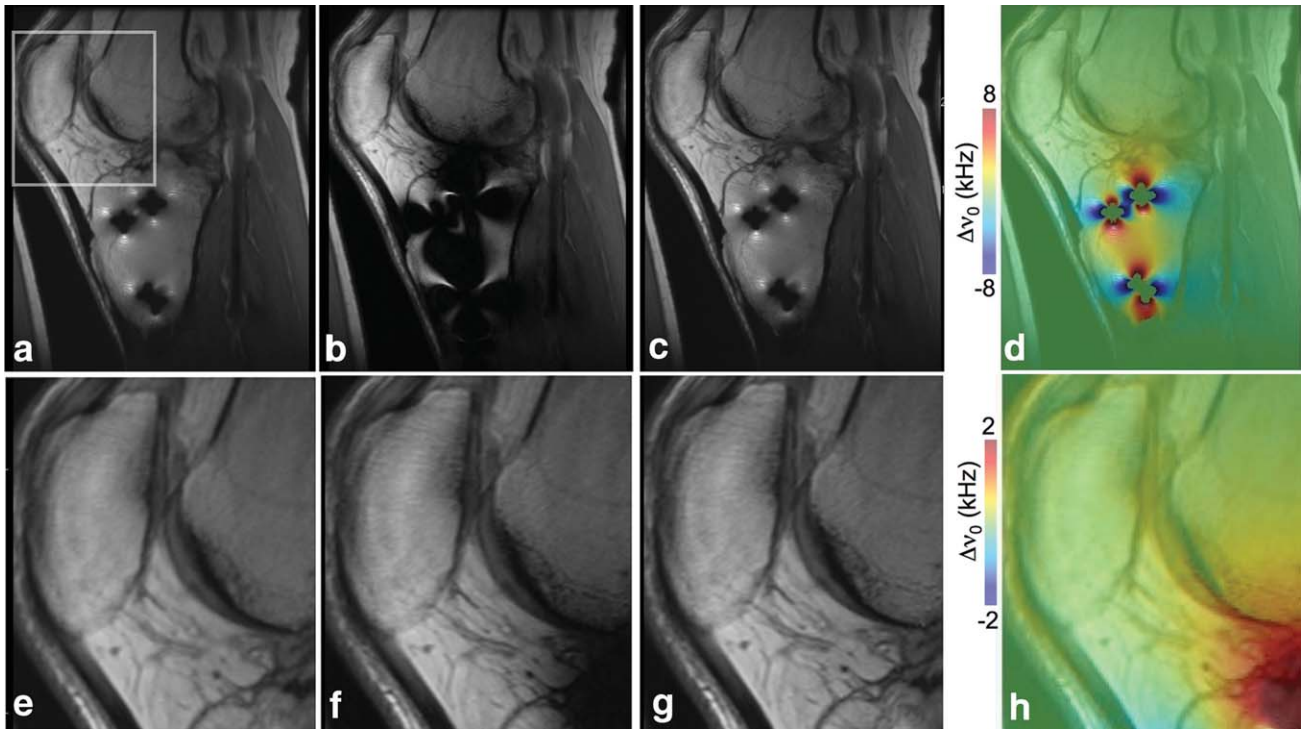

FIG. 3. Demonstration and correction of blurring from overlapping spectral profiles: (**a**) quadrature-summed composite image without blurring correction; (**b**) 3D-FSE image indicating native Fourier-encoded resolution; (**c**) corrected composite image. (**d**) Field map constructed from MAVRIC data. Zoomed views of the composite MAVRIC image (**e**), 3D-FSE image (**f**), corrected composite image (**g**), and field map (**h**) over the region is indicated in (**a**).

The presented method hinges on an earlier statement that SEMAC can simply be considered MAVRIC with a properly scaled Z-shim. Here, we describe how to determine the amplitude and effectively implement such a Z-shim to add z-selectivity to the MAVRIC technique.

Consider a MAVRIC acquisition with N_b spectral bins and a bin separation of Ω_b kHz. We desire to restrict the excited z FOV to ΔZ cm. This can be accomplished by applying the MAVRIC excitations under a z-gradient of amplitude $G_z = \frac{2\pi N_b \Omega_b}{\gamma \Delta Z}$. As in SEMAC, the z-gradient must also be turned on during the readout process to keep off-resonance effects limited to the RF bandwidth. Thus, this approach also adds VAT to the MAVRIC acquisition. Like SEMAC, readout filtration dictated by Eq. 3 is minimized using a high readout bandwidth ($\pm$125 kHz). Also like SEMAC, the resolution in the z-dimension of such an acquisition is not determined by the selective z-gradient amplitude, but rather by the extent of the k_z phase encodes. As multiple z-encodes are performed on each excited volume, the view angle is also much lower than that used in an equivalent 2D VAT experiment. Here, this hybrid method will be referred to as volume-selective 3D multi-spectral imaging (VS-3D-MSI).

METHODS

Images were acquired on 1.5-T and 3.0-T General Electric HDx (GE Healthcare, Milwaukee, WI) systems running 15.0 Signa software. All volunteers were scanned in accordance with site-specific Institutional Review Board policies.

All presented MAVRIC and VS-3D-MSI images were collected using $N_b = 24$ spectral bins with $\Omega_b = 1$ kHz bin separation, readout bandwidth of $\mathrm{BW_r} = \pm 125$ kHz, Gaussian RF spectral profiles with full width at half maximum ratio = 2.25 kHz, 2$\times$ ARC parallel imaging (20 calibration lines) in k_y, homodyne-reconstructed partial-Fourier acceleration (eight overscans) in k_y, and elliptical view ordering in the $k_y - k_z$ plane. Images were reconstructed using compiled Matlab (Natick, MA) software.

Images are presented from a number of implant scenarios. Phantom images demonstrating the method are presented from a cobalt-chromium/titanium total-hip replacement phantom at 1.5 T using an eight channel cardiac reception array. A direct in vivo comparison of the VS-3D-MSI and MAVRIC methods is performed on images acquired at 3.0 T near stainless steel ankle hardware using an eight-channel head reception array. Finally, three clinical cases are presented. First, images of a cobalt-chromium/titanium total hip replacement patient are used to demonstrate the clinical limitations of the MAVRIC technique in the absence of z-selectivity. In the other two cases, the SNR and z-selectivity advantages of the VS-3D-MSI technique are shown to produce high-diagnostic quality images near cobalt-chromium/titanium total hip and shoulder replacements. For these cases, conventional 2D-FSE images using established standard-of-care arthroplasty protocols (2) are shown in addition to the VS-3D-MSI images. All hip and shoulder images were acquired with a three-channel shoulder reception array.

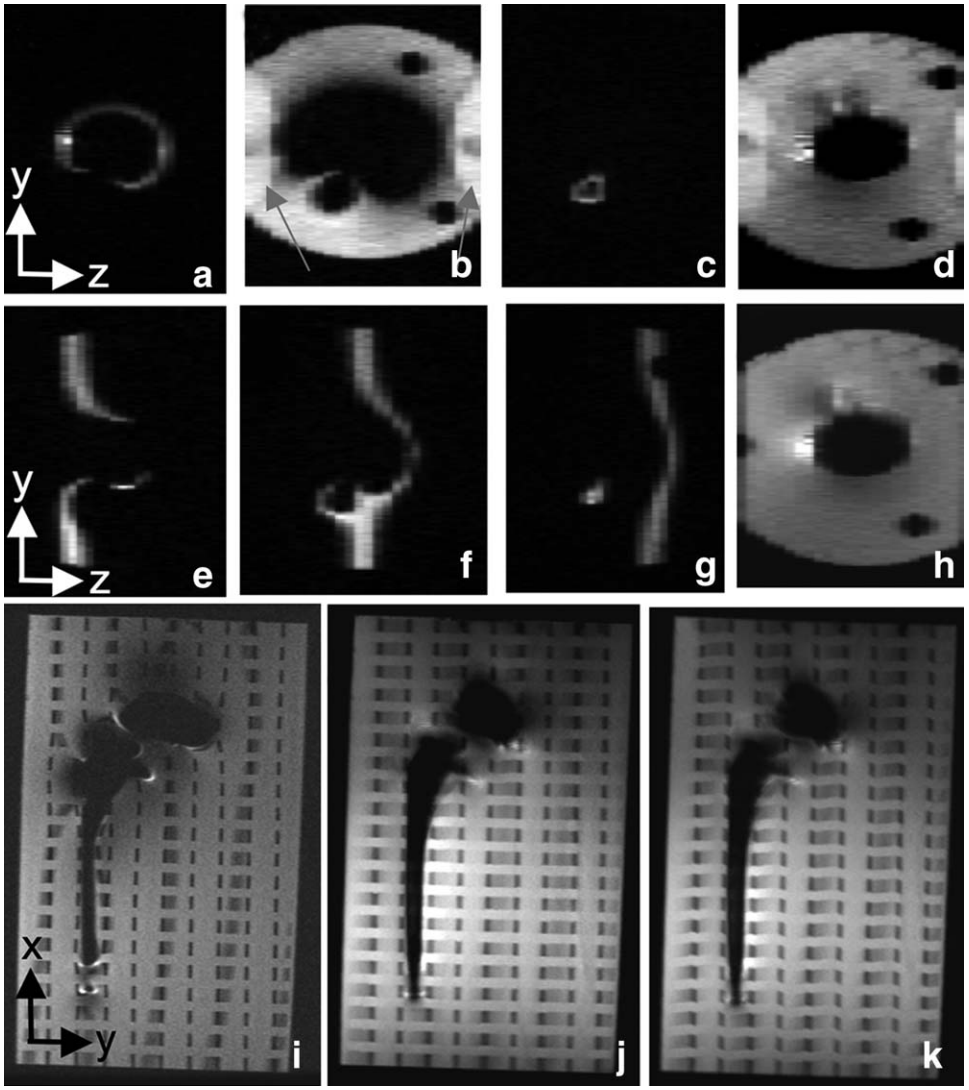

FIG. 4. Total hip replacement phantom at 1.5 T: (**a–d**) 4 kHz, 0 kHz, 4 kHz bins, and composite reformatted (coordinate axes indicate logical encoding directions) MAVRIC images. Arrows indicate aliasing in the k_z-encoded dimension. (**e–h**) 4 kHz, 0 kHz, 4 kHz bins, and composite-reformatted VS-3D-MSI images; (i–k) 2D-FSE, MAVRIC, and VS-3D-MSI in-plane images.

The acquisition parameters for all presented images are reported in Table 1.

RESULTS

Figure 3 demonstrates the correction of bin-overlap blurring. Here, MAVRIC images are displayed, though the applied deblurring algorithm remains identical for VS-3D-MSI images (the calculated field map will simply show the applied *Z*-shim in addition to the background field). Images are presented from the same implant scenario analyzed in Fig. 2 (Case 1 in Table 1). Uncorrected sum-of-squares images, 3D-FSE images, deblurred sum-of-squares images, and utilized field maps are displayed in (a,e), (b,f), (c,g), and (d,h), respectively. To illustrate the source of the field distortions, field maps are displayed as semitransparent color maps superimposed on the composite MAVRIC image. Close inspection of the zoomed images in (e–g) show that the blurring identified in the uncorrected image (e) is clearly repaired in the corrected image (g). After correction, the spatial resolution of the repaired image closely represents the native Fourier-encoded resolution represented by the on-resonance image (f). This blurring correction is implemented on all MAVRIC and VS-3D-MSI images presented throughout the rest of this work.

Figure 4a–f presents the variation of excitation volumes and composite images when applying a *z*-gradient in the presence of an implant-induced $\Delta\nu_0$ distribution. Here, a total hip replacement phantom fitted with an acrylic grid is imaged at 1.5 T (Case 2 in Table 1). The volumes (viewed in the k_y–k_z encoded plane) excited without the use of a *z*-gradient are displayed (a–c) for the −4 kHz, 0 kHz, +4 kHz spectral bins. A composite MAVRIC image is shown in (d). It is clear that the 0 kHz bin (b) in this case is susceptible to phase-encode aliasing in the *z*-dimension (arrows). When the appropriately scaled *z*-gradient is applied in the VS-3D-MSI images (e–h), the excited volumes are all selective in *z*, eliminating the threat of phase-encode aliasing

in this dimension. The reduction of aliasing is clearly visible in the composite images (d and h). Figure 4i–k displays the in-plane images using (i) 2D-FSE ($BW_r = \pm 125$ kHz), (j) MAVRIC, and (k) VS-3D-MSI. It is clear that both (j) and (k) correct the susceptibility artifacts found in (i). In particular, the curvature of the grid lines in the 2D-FSE image is removed in both the MAVRIC and VS-3D-MSI images. There is no significant change of the artifact reduction found in (j) when the z-selective process (k) is used. Examination of the plastic phantom gridlines in (k) shows a slight shear relative to those in (i) and (j). This is an anticipated effect of the VAT process and is easily identifiable in the displayed phantom images because its grid lines are aligned with the k_x- and k_z-encoded dimensions.

Figure 5 displays in vivo results near a stainless steel ankle hardware at 3 T (Case 3 in Table 1). Reformats (x, z) plane of 2D-FSE (a), MAVRIC (b), and VS-3D-MSI (c) images are presented. Notice the dramatic slice-selective distortions in the 2D-FSE image. Although the MAVRIC image (b) repairs these distortions, the lack of selectivity in the z-dimension is clearly evident by the aliasing of the toe region (arrow). The VS-3D-MSI image (c) repairs the susceptibility artifacts while also removing the aliasing in the k_z-encoded dimension. In-plane images for the 2D-FSE ($BW_r = \pm 125$ kHz), MAVRIC, and VS-3D-MSI acquisitions are also displayed in (d), (e), and (f), respectively. The dotted lines in (a–c) indicate the location of the corresponding in-plane images. Images (g–i) present zoomed views of (d–f) localized to the region indicated by the box in (f). Again, the significant 2D-FSE distortions of the bone structure near the metal hardware are repaired in both the MAVRIC and VS-3D-MSI images.

A few important characteristics of the MAVRIC versus VS-3D-MSI images are illustrated here. First, the shearing effect seen in the gridlines of Fig. 4k is not easily identifiable in the in vivo VS-3D-MSI images Fig. 5c,f. Second, there is no dramatic change in the resolution between the MAVRIC and VS-3D-MSI images, which indicates that the high readout bandwidth (±125 kHz) is satisfactorily mitigating the blurring filter expressed in Eq. 3. Third, close inspection of the air regions of (e) and (f) shows that the MAVRIC image has more residual in-plane signal aliasing after parallel image reconstruction [an arrow in (e) indicates such aliasing]. Both images were processed through the same reconstruction pipeline. The improved performance in the VS-3D-MSI image can be explained by the amount of in-plane signal available for each spectral bin's independent reconstruction process. As demonstrated in Fig. 4, the amount of in-plane signal is consistently larger across VS-3D-MSI spectral bins. This provides more information to the data-driven autocalibration process used in ARC and results in more successful unaliasing of the k_y undersampled data in VS-3D-MSI images.

Although Fig. 5 demonstrates VS-3D-MSI's removal of through-plane aliasing found in MAVRIC images, the displayed aliasing is not likely to be diagnostically significant. In a clinical environment, it is not difficult to find cases where such aliasing is of severe diagnostic impact. Figure 6a presents an in-plane MAVRIC image of a total right hip arthroplasty patient at 1.5 T (Case 4 in Table 1). Despite the marked susceptibility artifact reduction, aliased through-plane signal destroys the image

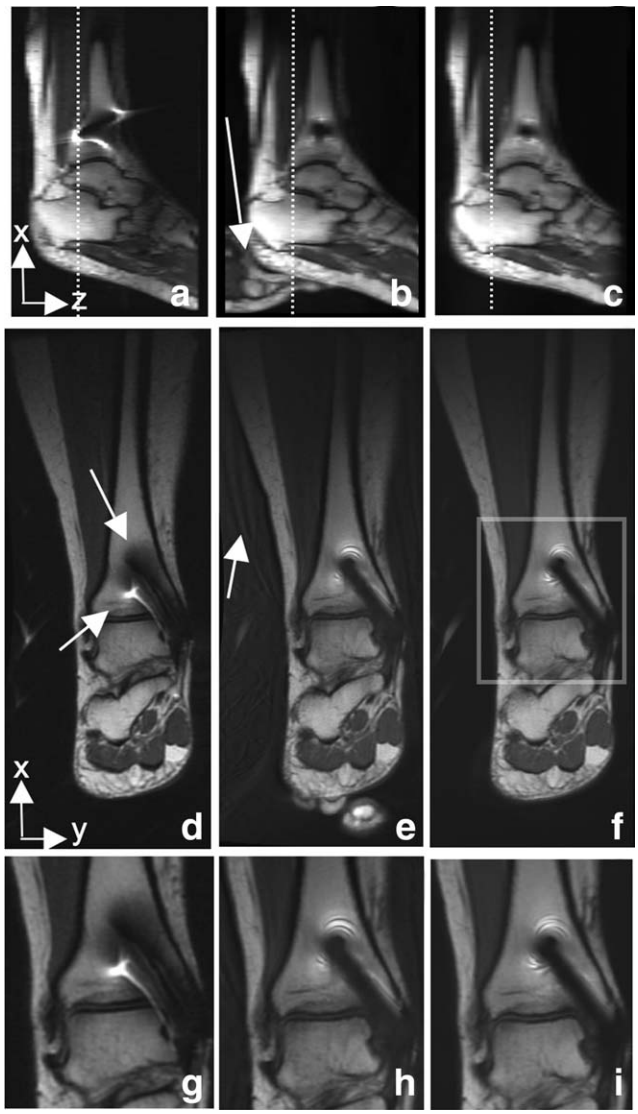

FIG. 5. Stainless steel ankle screw at 3 T: reformatted (coordinate axes indicate logical encoding directions) 2D-FSE (**a**), MAVRIC (**b**), and (**c**) VS-3D-MSI images. Arrows indicate aliasing in the k_z-encoded dimension of the MAVRIC image. (**d–f**) In-plane images indicated by dotted line in (**a–c**). Arrows indicate significant distortions in the 2D-FSE (**d**) image that are corrected in both the MAVRIC (**e**) and VS-3D-MSI (**f**) images. (**g–i**) Zoomed views of (**d–f**) localized to the region indicated by the box in (**f**).

integrity near the acetabular head of the implant. A reformat of this MAVRIC acquisition is presented in (b) and clearly illustrates the problematic aliasing through plane signal. Increasing the number of z-encodes to eliminate this aliasing would result in clinically unacceptable acquisition times. Images near a similar total left hip replacement (Case 5 in Table 1) are presented for (c) and (e) VS-3D-MSI and standard-of-care (d) 2D-FSE ($BW_r = \pm 100$ kHz) and acquisitions. Figure 6c presents a reformat of the VS-3D-MSI image that clearly eliminates the through-plane aliasing seen in (b). The significant geometric distortions in the 2D-FSE image (d) are greatly reduced in the VS-3D-MSI (e) image while simultaneously eliminating the detrimental

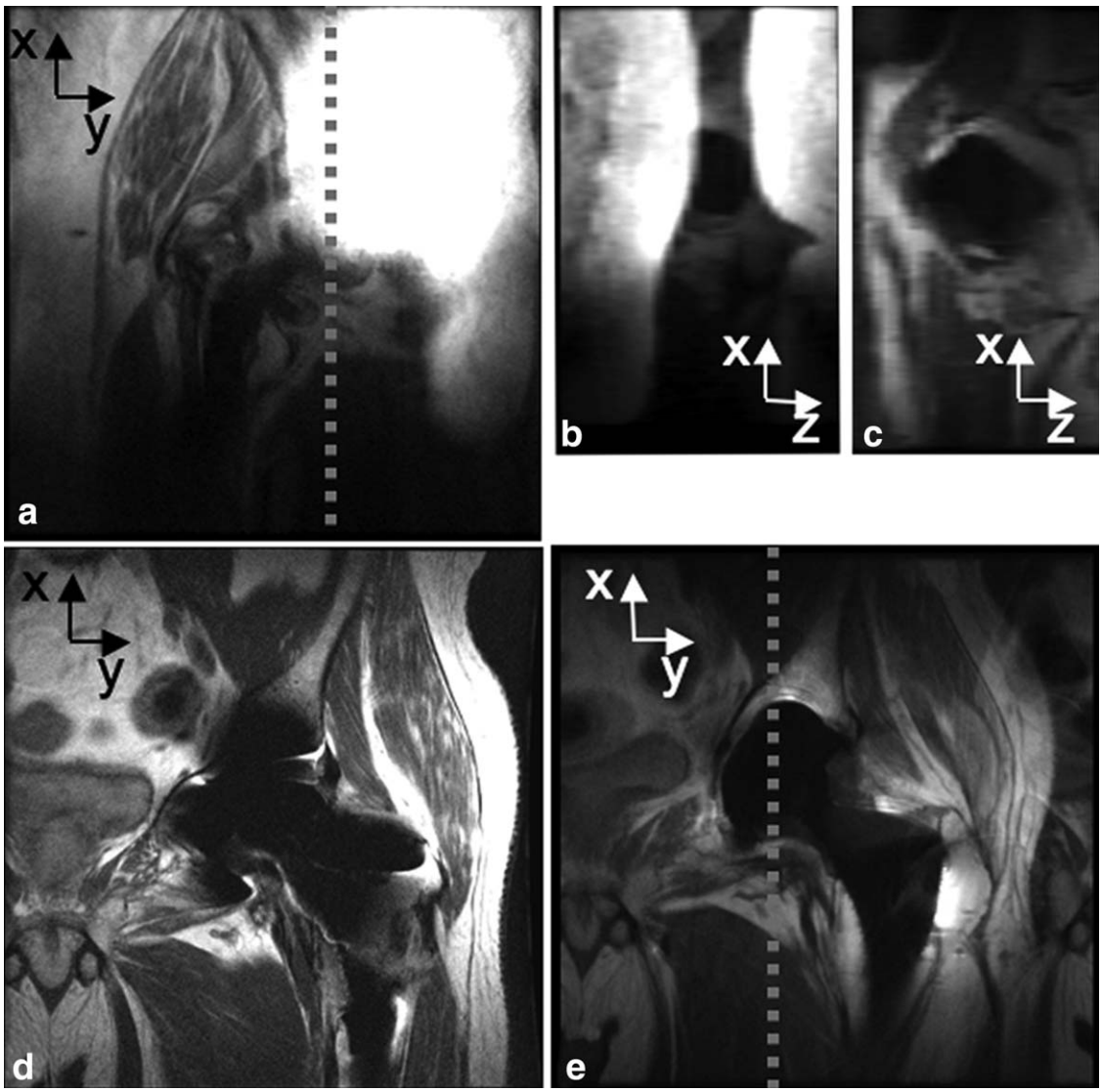

FIG. 6. Clinical utility of the VS-3D-MSI method on total hip replacements. a: MAVRIC image of a total hip replacement where through-plane aliasing overwhelms the signal near the implant. b: Reformat (coordinate axes indicate logical encoding directions) of the MAVRIC image displayed in (**a**), indicated through dotted line. c: Reformat of a VS-3D-MSI image on another total hip replacement patient where the aliased signal seen in (**b**) has now been removed. d: In-plane 2D-FSE image of the implant displayed in (**c**). e: In-plane VS-3D-MSI image of the case displayed in (**d**), with dotted line indicating the position of the reformatted image in (**c**). In-plane (k_y) aliasing remains in the VS-3D-MSI image (**e**), but is suppressed in the clinical 2D-FSE images (**d**) via the application of extra phase encodes embedded in the signal-averaging process (i.e., k_y oversampling).

through-plane aliasing that would be introduced with a similar MAVRIC acquisition.

The images in Fig. 7 present (a) standard-of-care 2D-FSE ($BW_r = \pm 100$ kHz) and (b) VS-3D-MSI images near a total shoulder replacement at 1.5 T (Case 6 in Table 1). The oblique scan plane imaged in these acquisitions was not achievable with MAVRIC due to through-plane aliasing. While a significant amount of signal near the implant has been distorted out of the 2D scan plane in (a), the VS-3D-MSI image (b) offers spatially accurate visualization of anatomy near the implant that is unavailable using any conventional MR methods.

The clinical standard-of-care 2D-FSE scans presented in Figs. 6–7 suppress in-plane (k_y) aliasing by embedding extra k_y encodes within the signal-averaging process. Because of scan time constraints, MAVRIC, SEMAC, and VS-3D-MSI are not yet capable of applying such in-plane-aliasing prevention schemes.

DISCUSSION

A hybrid method that incorporates advantageous elements of both the SEMAC and MAVRIC imaging techniques has been introduced. The slab selectivity of SEMAC has been fused with the smooth bin combination and higher SNR spectral strategy implemented by MAVRIC. In addition, a technique to remove unwanted blurring introduced by such a spectral overlap strategy has been described and

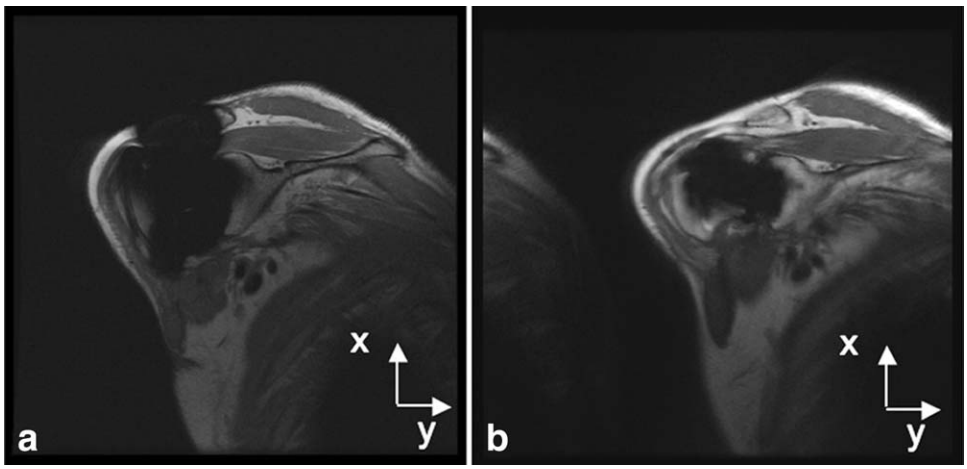

FIG. 7. Clinical utility of the VS-3D-MSI method on a total shoulder replacement. a: 2D-FSE image of a total shoulder replacement. b: VS-3D-MSI image of the same replacement. The oblique imaging plane used in acquiring these images was not feasible with the MAVRIC technique, because of excessive through-plane (k_z) aliasing. In-plane (k_y) aliasing remains in the VS-3D-MSI image (**b**), but is suppressed in the clinical 2D-FSE images (**a**) via the application of extra phase encodes embedded in the signal-averaging process (i.e., k_y oversampling).

demonstrated. The resulting VS-3D-MSI technique has been conceptually demonstrated and its utility is proven in a clinical setting. Using the VS-3D-MSI method, images of previously unattainable image quality have been acquired on total hip and total shoulder arthroplasty patients in clinically viable acquisition times. The presented methods allow for high-quality spatially accurate diagnostic imaging near a wide variety of metal implants.

VS-3D-MSI images presented in this work were acquired with acquisition times ranging from roughly 7 to 12 min, depending on the used acquisition parameters. Partial-Fourier, autocalibrated parallel imaging, and $k_y - k_z$ corner-removal schemes have been implemented to minimize this scan time. Without any acceleration, each of the displayed images would have ranged from roughly 20 to 50 min in total acquisition time. The significant undersampling required to achieve such acceleration is one of the motivations to maximize SNR with the applied spectral windowing strategy. Although a variety of slight parameter alterations could be used to further reduce these scan times (such as increasing the ETL, reducing the TR period, reducing z-encodes, and/or reducing in-plane resolution), VS-3D-MSI images will typically require slightly more acquisition time than conventional imaging strategies. Regardless, the advantages of accessing previously unavailable anatomy near metal hardware may often prove worth the added scan time requirements.

In vivo imaging with both the SEMAC and VS-3D-MSI techniques has shown little adverse effects of the VAT method. The use of high-bandwidth readouts in both techniques minimizes the blurring effects of the readout filtration expressed in Eq. 3. The VAT-induced shear identified in Fig. 4 has not been identifiable in vivo. This is because imaging of anatomy does not provide the hard and consistent boundaries that allow for visualization of the shear of the readout in the $k_z - k_x$ plane. Even though there does not appear to be any pressing motivation for doing so, removal of the shear could be accomplished through regridding of the acquired k_x and k_z lines.

Initial clinical investigations suggest that the SNR of VS-3D-MSI images is often high enough to seek further undersampled acceleration. Unfortunately, available coil geometries restrict the amount of parallel imaging acceleration feasible in a given spatial dimension. Moving toward the sliding z-encoded FOV implemented with SEMAC could offer a path to spend extra SNR while slightly reducing scan times. Further $k_y - k_z$ undersampling of MAVRIC has also been demonstrated by exploiting the redundant spatial information contained in overlapping spectral bins (23). In the face of such additional undersampling, more sophisticated spectral bin combination strategies, such as those explored to maximize SNR in SEMAC images (24), could be implemented in the VS-3D-MSI method. In particular, empty spectral bins containing only noise could be identified and removed from the summation process.

In this work, initial images were demonstrated with the VS-3D-MSI technique at 3 T. The image displayed in Fig. 5 shows significant artifact reduction using the VS-3D-MSI method when compared with 2D-FSE. This suggests that imaging near smaller hardware fixations (screws, etc.) may be feasible at 3 T and that the residual artifacts in VS-3D-MSI (or SEMAC and MAVRIC) images will be far more modest than those in 2D-FSE. However, further studies will be required to assess the viability of imaging larger total joint assemblies at 3 T. Initial investigations with the MAVRIC technique have identified significant B_1 radiofrequency field perturbations near total hip replacements at 3 T (25). Because of specific absorption rate constraints, the use of high-bandwidth spin-echo refocussing pulses adds further complexity to the application of the presented methods at 3 T.

In conclusion, the VS-3D-MSI method provides further advancement toward routine MR imaging near embedded metal hardware. By fusing the MAVRIC and SEMAC techniques, high-quality clinical images have been demonstrated on total hip and total shoulder replacement patients.

ACKNOWLEDGMENTS

The authors thank Dr. Reed Busse for valuable discussions on 3D-FSE pulse-sequencing techniques, and Dr. Phil Beatty for providing the ARC parallel imaging reconstruction code.

REFERENCES

1. White L, Kim J, Mehta M, Merchant N, Schweitzer M, Morrison W, Hutchinson C, Gross A. Complications of total hip arthroplasty: MR imaging—initial experience. Radiology 2000; 215:254–262.
2. Potter HG, Nestor BJ, Sofka CM, Ho ST, Peters LE, Salvati EA. Magnetic resonance imaging after total hip arthroplasty: evaluation of perioprosthetic soft tissue. J Bone Joint Surg Am 2004;86:1947–1954.
3. Toms A, Marshall T, Cahir J, Darrah C, Nolan J, Donell S, Barker T, Tucker J. MRI of early symptomatic metal-on-metal total hip arthroplasty: a retrospective review of radiological findings in 20 hips. Clin Radiol 2008;63:49–58.
4. Ramos-Cabrer P, van Duynhoven J, der Toorn AV, Nicolay K. MRI of hip prostheses using single-point methods: in vitro studies towards the artifact-free imaging of individuals with metal implants. Magn Reson Imaging 2004;22:1097–1103.
5. Venook RD, Matter NI, Ramachandran M, Ungersma SE, Gold GE, Giori NJ, Macovski A, Scott GC, Conolly SM. Prepolarized magnetic resonance imaging around metal orthopedic implants. Magn Reson Med 2006;56:177–186.
6. Butts K, Pauly JM, Daniel BL, Kee S, Norbash A. Management of biopsy needle artifacts: techniques for RF-refocused MRI. J Magn Reson Imaging 1999;9:586–595.
7. Olsen R, Munk P, Lee M, Janzen D, MacKay AL, Xiang QS, Masri B. Metal artifact reduction sequence: early clinical applications. Radiographics 2000;20:699–712.
8. Skare S, Andersson J. Correction of MR image distortions induced by metallic objects using a 3D cubic B-spline basis set: application to stereotactic surgical planning. Magn Reson Med 2005;54:169–181.
9. Koch KM, Lorbiecki JE, Hinks RS, King KF. A multispectral three-dimensional acquisition technique for imaging near metal implants. Magn Reson Med 2009;61:381–390.
10. Lu W, Pauly KB, Gold GE, Pauly J, Hargreaves B. SEMAC: slice encoding for metal artifact correction in MRI. Magn Reson Med 2009;62: 66–76.
11. Chen CA, Chen W, Goodman SB, Hargreaves BA, Koch KM, Lu W, Brau AC, Draper CE, Delp SL, Gold GE. SEMAC and MAVRIC for artifact-corrected MR imaging around metal in the knee. In: Proceedings of the ISMRM, Stockholm, Sweden, 2010. p 130.
12. Koff M, Koch K, Potter H. Magnetic resonance imaging of periprosthetic tissues in the presence of joint arthroplasty. In: Proceedings of the ISMRM, Stockholm, Sweden, 2010, p 131.
13. Gold GE, Vasanawala SS, Lu W, Chen CA, Chen W, Pauly JM, Pauly KB, Goodman SB, Hargreaves BA. MRI near metallic implants using SEMAC: initial clinical experience. Proceedings of the ISMRM, Stockholm, Sweden, 2010. p. 893.
14. Cho ZH, Kim DJ, Kim YK. Total inhomogeneity correction including chemical shifts and susceptibility by view angle tilting. Med Phys 1988;15:7–11.
15. Pauly KB, Gold GE. Correction of slice profile distortion from metallic devices. Proceedings of the ISMRM, Seattle, WA, 2006. p 2380.
16. Beatty P, Brau A, Chang S, Joshi S, Michelich C, Bayram E, Nelson T, Herfkins R, Brittain J. A method for autocalibrating 2D-accelerated volumetric parallel imaging with clinically practical reconstruction times. Proceedings of the ISMRM, Berlin, Germany, 2007. p 1749.
17. Brau A, Beatty P, Skare S, Bammer R. Comparison of reconstruction accuracy and efficiency among autocalibrating data-driven parallel imaging methods. Magn Reson Med 2008;59:382–395.
18. Chen W, Beatty P, Koch KM, Brau A. Parallel MRI near metallic implants. Proceedings of the ISMRM, Honolulu, HA, 2009. p 2783.
19. Hargreaves BA, Chen W, Lu W, Alley MT, Gold GE, Brau ACS, Pauly JM, Butts-Pauly K. Accelerated slice-encoding for metal artifact correction. J Magn Reson Imag 2010;31:987–996.
20. Busse R, Brau A, Vu A, Michelich C, Bayram E, Kijowski R, Reeder S, Rowley H. Effects of refocusing flip angle modulation and view ordering in 3D fast spin echo. Magn Reson Med 2008;60:640–649.
21. Hernando D, Koch KM, King KF, Liang Z. Generalized reconstruction of multi-spectral MR acquisitions for imaging near metal implants. Proceedings of the ISMRM, Honolulu, HA, 2009. p 2860.
22. Pauly JM, Le-Roux P, Nishimura D, Macovski A. Parameter relations for the Shinnar-Le Roux selective excitation pulse design algorithm. IEEE Trans Med Imaging 1991;10:53–65.
23. Lai P, Chen W, Koch K, Brau A. kf ARC reconstruction for improving MRI around metal using MAVRIC. Proceedings of the ISMRM, Stockholm, Sweden, 2010. p 133.
24. Lu W, Gold GE, Pauly JM, Hargreaves BA. Noise considerations in slice encoding for metal artifact correction. Proceedings of the ISMRM, Honolulu, HA, 2009. p 2781.
25. Koch K, King K, McKinnon G. B1 Effects when imaging near metal implants at 3 T. Proceedings of the ISMRM, Stockholm, Sweden, 2010. p 3082.